

Identification of vanadium dopant sites in the Metal-Organic Framework DUT-5(Al)

Received 00th January 20xx,
Accepted 00th January 20xx

DOI: 10.1039/x0xx00000x

Kwinten Maes^a, Lisa I. D. J. Martin^a, Samira Khelifi^a, Alexander Hoffman^b, Karen Leus^c, Pascal Van Der Voort^c, Etienne Goovaerts^d, Philippe F. Smet^a, Veronique Van Speybroeck^b, Freddy Callens^a and Henk Vrielinck^{a*}

Studying the structural environment of the V^{IV} ions doped in the metal-organic framework (MOF) DUT-5(Al) ((Al^{III}OH)BPDC) with electron paramagnetic resonance (EPR) reveals four different vanadium-related spectral components. The Spin-Hamiltonian parameters are derived by analysis of X-, Q- and W-band powder EPR spectra. Complementary Q-band Electron Nuclear Double Resonance (ENDOR) experiments, Scanning Electron Microscopy (SEM), Energy Dispersive X-ray spectroscopy (EDX), X-Ray Diffraction (XRD) and Fourier Transform InfraRed (FTIR) measurements are performed to investigate the origin of these spectral components. Two spectral components with well resolved ⁵¹V hyperfine structure are visible, one corresponding to V^{IV}=O substitution in a large (or open) pore and one to a narrow (or closed) pore variant of this MOF. Furthermore, a broad structureless Lorentzian line assigned to interacting vanadyl centers in each other's close neighborhood grows with increasing V-concentration. The last spectral component is best visible at low V-concentrations. We tentatively attribute it to (V^{IV}=O)²⁺ linked with DMF or dimethylamine in the pores of the MOF. Simulations using these four spectral components convincingly reproduce the experimental spectra and allow to estimate the contribution of each vanadyl species as a function of V-concentration.

1. Introduction

Metal-organic frameworks (MOFs) are porous crystalline materials constructed of metal-inorganic units connected with organic linker molecules. By choosing the right building blocks their structural characteristics, like crystal lattice, pore shape and size, and physicochemical properties can be adjusted, giving MOFs a competitive advantage over other porous materials, like zeolite frameworks or activated carbon. Various applications for MOFs have been demonstrated or are currently being explored, e.g. in catalysis, sensing, gas storage, separation and adsorption⁴⁻⁹. Our interest in these materials started with the MOF MIL-47¹⁰ (MIL = Matériaux de l'Institut Lavoisier), consisting of V^{IV}=O nodes connected by BDC (1,4-benzenedicarboxylate) linkers, that proved to be an efficient catalyst in the liquid phase oxidation of cyclohexene⁵. However, this framework is not completely stable in aqueous environment. Therefore, alternatives were investigated, like the more stable isorecticular structures MIL-53(Al) ((Al^{III}OH)BDC)¹¹ and DUT-5(Al) ((Al^{III}OH)BPDC, BPDC = biphenyl-4,4'-

dicarboxylate) (DUT = Dresden University of Technology)¹² doped with catalytically active V^{IV}. This mixing of metals in MOFs opens a wide variety of new customization options¹³.

MIL-53(Al) has been extensively studied over the last 15 years. Its framework has the property generally referred to as "breathing": it can reversibly change between a state with open, large pores (**lp**) and a state with closed, narrow pores (**np**). Some other representatives of the MIL-53 family (M^{III}(OH)BDC) have also been reported to exhibit breathing (M = V, Cr, Ga)¹⁴⁻¹⁶, while others do not (M = Fe, Sc)^{17,18}. In general these transitions can be induced by external triggers, like temperature, mechanical pressure and exposure to (and the presence of) certain gasses, most notably water vapor and CO₂. After solvothermal synthesis, the as synthesized structures (**as**) do not immediately exhibit breathing. Solvent and excess linker molecules that block the pores need to be removed first by solvent extraction or calcination (i.e. activation of the MOF). Studying MIL-53(Al) doped with vanadium, we found that the electron paramagnetic resonance (EPR) spectrum of vanadyl defects (in which V^{IV} has a 3d¹ electron configuration with effective electron spin S = 1/2), replacing regular Al-OH nodes in the framework, is a very sensitive marker for the framework state^{1, 19, 20}. By monitoring X-ray diffraction (XRD), Fourier Transform Infrared (FTIR), and multifrequency EPR spectroscopy *in situ* during breathing transformations, we were able to isolate and completely characterize the EPR spectra for V^{IV}=O defects in four different states of the MIL-53(Al) framework. When stored at room temperature (RT) and ambient air atmosphere, activated MIL-53(Al) adopts a

^a Department of Solid State Sciences, Ghent University, Krijgslaan 281-S1, B-9000 Gent, Belgium. E-mail: henk.vrielinck@ugent.be

^b Center for Molecular Modeling, Ghent University, Technologiepark 903, 9052 Zwijnaarde, Belgium.

^c Department of Chemistry, Ghent University, Krijgslaan 281-S3, B-9000 Gent, Belgium

^d Department of Physics, University of Antwerp, Universiteitsplein 1, B-2610 Antwerp, Belgium

Electronic Supplementary Information (ESI) available: [details of any supplementary information available should be included here]. See DOI: 10.1039/x0xx00000x

hydrated **np** framework state (**np-h**). Upon heating, the framework dehydrates (**np-d**) before making the transition to the **lp** state. A detailed study of the $V^{IV}=O$ EPR spectra for the **np-h** and **as** states reveals that at least two slightly distinct dopant sites co-exist, in contrast to only one dopant site for the other two states. Upon fully replacing Al with V as metal node, MIL-53(V) is formed, which takes a special position: when activated by solvent extraction without changing the oxidation state of the metal ions (V^{III}), it exhibits breathing. However, with calcination of the sample the metal-inorganic backbones transform into vanadyl ($V^{IV}=O$) chains, and the framework adopts a rigid **lp** structure, that of MIL-47¹⁰. Remarkably, during this transition the EPR spectrum always exhibits a broad signal without resolved ^{51}V hyperfine structure, which is resolved for isolated vanadyl centers in the framework.

DUT-5(Al) has the same topology and metal-inorganic building blocks as MIL-53(Al), but with a longer linker molecule. It remains in a rigid open pore structure, thus it does not exhibit breathing²¹. On the contrary, in ($V^{IV}=O$)BPDC, i.e. COMOC-2(V) (COMOC = Centre for Ordered Materials, Organometallics and Catalysis, Ghent University)²², we recently detected a new type of CO_2 -triggered breathing. Only a part of the framework changes state as a function of CO_2 pressure, while the rest remains in the original **lp** state. The “breathing” part of the framework first transforms to a **np** state and then opens again at higher pressures to a **lp** state, which is markedly different from the original. Even for MOFs that do not exhibit breathing, both the open and closed pore framework can exist. For example DUT-4 synthesized in DMF always gives a **lp** phase. On the contrary, when it is hydrothermally synthesized a **np** phase, also called MIL-69, is formed^{12, 21, 23}.

In our earlier investigation of mixed $(Al^{III}OH)_x(V^{IV}=O)_{1-x}$ BPDC MOFs, we detected several $V^{IV}=O$ spectral components in the EPR spectra^{2, 3}. At low V-concentrations two components were visible. One shows the typical characteristics of $V^{IV}=O$ substituting for regular Al-OH units in MIL-53(Al) in the **lp** framework state. We determined the spin-Hamiltonian parameters for this spectral component and provided evidence for its assignment. The other one present at low V-concentrations dominates the EPR spectrum recorded on the sample in air. However, it proved difficult to completely isolate it. Its spin-Hamiltonian parameters are unlike any parameters for vanadyl centers in MIL-53(Al):V.

At higher concentrations of V in the framework of DUT-5(Al), additional spectral components were visible. The contribution of a broad single line without hyperfine (HF) structure steadily grows with increasing V-concentration. Secondly, we observed the z-component HF pattern of an additional vanadyl center, with EPR characteristics pointing to substitution for framework Al-OH in a **np** state. Re-examination of the XRD patterns of these MOFs seemed to support this a priori unexpected identification, in view of the rigidity of the DUT-5 framework and the fairly low (9 %) global V-concentrations at which a **np** state would already occur.

In the present paper, we report on a detailed spin-Hamiltonian analysis of all four spectral components. Simulations of the isolated experimental EPR spectra show very good agreement.

A decomposition using these four components is performed. Furthermore, we aim at further identifying the dominant spectral components in the powder EPR spectra of DUT-5(Al):V by analysis of X-, Q- and W-band EPR spectra complemented with Q-band Electron Nuclear Double Resonance (ENDOR) experiments, Scanning Electron Microscopy (SEM) images combined with Energy Dispersive X-Ray Spectroscopy (EDX), FTIR and XRD. Next to a concentration series of $VOSO_4$ doped DUT-5(Al) samples³, samples doped in different ways and/or in different synthesizing conditions have also been investigated in search of the identification of specific EPR signals.

Table 1: Overview of the samples. Samples with an asterisk * are not discussed here, but were the subject of previous work. Aluminum and vanadium concentrations for the concentration series samples were measured by Inductively Coupled Plasma – Optical Emission Spectrometry (ICP-OES) and Inductively Coupled Plasma – Mass Spectrometry (ICP-MS) respectively³. Vanadium concentrations for the other samples were estimated based on the precursor materials used in the synthesis.

Sample	V(%)	Label
COMOC-2(V)	100	COMOC-2
COMOC- $V_{0.81}Al_{0.19}$ *	81	CS-01
COMOC- $V_{0.66}Al_{0.34}$ *	66	CS-02
COMOC- $V_{0.46}Al_{0.54}$	46	CS-03
COMOC- $V_{0.23}Al_{0.77}$	23	CS-04
COMOC- $V_{0.09}Al_{0.91}$	9	CS-05
COMOC- $V_{0.07}Al_{0.93}$	7	CS-06
COMOC- $V_{0.03}Al_{0.97}$	3	CS-07
COMOC- $V_{0.01}Al_{0.99}$	1	CS-08
DUT-5(Al)*	0	DUT-5
DUT-5(Al) 1 % VCl_3	1	T- VCl_3
$VOSO_4$ + DUT-5(Al)	1	T- $VOSO_4$
$VOSO_4$ + DMF	4	S-DMF-01
$VOSO_4$ + DMF + H_2 BPDC	4	S-DMF-02
Calcined DUT-5(Al) 1 % VCl_3	1	T- VCl_3 -H
Calcined COMOC- $V_{0.01}Al_{0.99}$	1	CS-08-H
Calcined COMOC- $V_{0.03}Al_{0.97}$	3	CS-07-H
Calcined COMOC- $V_{0.09}Al_{0.91}$	9	CS-05-H

2. Experimental

2.1 Synthesis of the materials

The synthesis of the DUT-5(Al):V concentration series was described by Depauw et al.³. A mixture of dimethylformamide (DMF), H_2 BPDC and different ratios of the metal salt vanadium oxide sulphate ($VOSO_4 \cdot H_2O$) and aluminum nitrate ($Al(NO_3)_3 \cdot 9H_2O$) were sealed in a flask, slowly heated to 421 K and kept at this temperature while stirring for 16 h. The crystalline material was filtrated and washed with DMF, methanol and acetone. Solvents were removed by keeping the sample at 393 K under vacuum for 2 h. The labels for the concentration series samples are in agreement with those given in Depauw et al.³, CS-01 being the sample with the highest V-concentration (81 %) and CS-08 with the lowest concentration (1 %). For comparison, a similar mixed-metal MOF has been synthesized, using VCl_3 as metal dopant salt instead of

VOSO₄•H₂O, following the same procedure described above (labelled T-VCl₃). Another sample was made where VOSO₄•H₂O was diluted in DUT-5(Al) by mixing 1 % of VOSO₄ and 99 % of DUT-5(Al) in DMF, stirring for 10 minutes in a temperature controlled (421 K) reaction vessel (labelled T-VOSO₄). Furthermore, a calcination step was performed on four samples. T-VCl₃-H was heated for 16 h at 425 K. CS-08-H, CS-07-H and CS-05-H were heated for 14 h at 525 K. Finally, frozen solutions of VOSO₄•H₂O in DMF and DMF + H₂BPDC have also been investigated. Table 1 summarizes the labels of the samples that were investigated in this study.

2.2 EPR measurements and analysis

All EPR and ENDOR measurements were recorded in continuous wave (CW) mode.

X-band EPR was performed with two different setups. Most X-band spectra were recorded using a Varian E-line spectrometer with a standard rectangular cavity (TE102 mode), a HP 5342A microwave frequency counter, and a Bruker NMR ER 035 M Gaussmeter, using diphenyl picrylhydrazyl (DPPH; $g = 2.0036$) for field calibration. Spectra were recorded at RT, 5 mW microwave power, 10 kHz modulation frequency and 0.2, 0.4 or 1.0 mT modulation amplitude. Some of the X-band EPR measurements were performed using a Bruker ESP300E spectrometer equipped with an ER 4102-ST rectangular cavity or an ER 4114HT high-temperature resonator, a HP5350 B frequency counter and a Bruker NMR ER 035M Gaussmeter, again using DPPH for field calibration. Spectra were recorded with the same conditions as in the Varian setup, but with 100 kHz modulation frequency. All spectra were frequency normalized to 9.5 GHz by a field shift, because the field span of the EPR spectrum is largely determined by the HF structure.

A Bruker ElexSys E500 spectrometer was used for the Q-band EPR and ENDOR measurements, equipped with an Oxford Instruments CF935 He-flow cryostat (2-300 K). A Pendulum CNT-90XL frequency counter and a Bruker NMR ER 035M Gaussmeter were used to measure microwave frequency and magnetic field, respectively. The g_{\perp} component of the CO₃³⁻ radical in irradiated calcite powder ($g = 2.0031$)²⁴ was used as a reference for field calibration. All spectra are normalized to 34 GHz frequency. Spectra were recorded both at RT and at 10 K. At RT, 5 mW microwave power was used with 100 kHz modulation frequency and 0.2 or 0.4 mT modulation amplitude. At 10 K, 0.0063 mW microwave power was used with 12.5 kHz modulation frequency and 0.4 mT modulation amplitude. ENDOR spectra were recorded with 0.25 mW microwave power, 200 W RF power and 250 kHz modulation depth. High intensity ENDOR signals were observed when the sample was inserted (quenched) in a precooled cavity, while signals were weak if the sample was slowly cooled starting from RT in the cavity. Simulations of EPR and ENDOR spectra were performed using the Easyspin toolbox (version 5.2.27) for MATLAB²⁵.

For the W-band (94 GHz) measurements a Bruker ElexSys E680 setup was used. EPR spectra were recorded at RT with 100 kHz modulation frequency, 0.8 mT modulation amplitude and 0.044 mW microwave power.

For X-band EPR measurements, powder samples were placed in one-end closed quartz tubes (5 mm outer diameter), either in ambient air or evacuated by continuous pumping ($p \approx 30$ Pa). For the Q-band EPR measurements, powder samples were also placed in quartz tubes (typically 2 mm outer diameter). In both microwave bands, approximately equal masses were used within the concentration series, allowing comparison of absolute EPR signal intensities. The spectra were recorded either with the samples in air, under vacuum by continuously pumping the sample tube, or by flushing the cavity with He gas (N50: $\geq 99.99\%$ mole). Under the latter two conditions, identical spectra were obtained in all studied cases.

2.3 Other characterization techniques

SEM images were obtained using a Thermo Fisher Scientific QUANTA 200F system operating at a pressure of 5×10^{-5} Pa. For element mapping a Hitachi S3400-N (back-scattered electron images) with connected Thermo Fisher Scientific Noran 7 EDS system was used, operating at a pressure of 20 Pa. For both setups the spectra were measured using 20 kV acceleration voltage. EDX spectra were processed using the Thermo Fisher Scientific NSS 3 software. Element mapping in Figure S6 in supporting information is based on the following lines: Al K α – 1.486 keV; C K α – 0.277 keV; O K α – 0.525 keV; V K α – 4.953 keV.

Powder XRD in air was carried out on a Siemens D5000 diffractometer equipped with a Cu anode X-ray source (Cu K α , $\lambda = 1.5406$ Å).

A Bruker Vertex-80v spectrometer equipped with a single bounce attenuated total reflection (ATR) unit with a diamond ATR crystal was used for measuring FTIR spectra in the 100-6000 cm⁻¹ range in an evacuated sample compartment (~ 200 Pa).

2.4 Computational details

Theoretical IR spectra of the **np** and **lp** phases of DUT-5(Al) and COMOC-2(V) were determined via static density functional theory (DFT) calculations with the Vienna Ab initio Simulation Package (VASP)²⁶. The calculations were performed at the PBE level of theory²⁷ including Grimme's D3 dispersion corrections²⁸ with Becke-Johnson damping²⁹. The projector-augmented wave method was applied³⁰ using a plane wave basis set with a cutoff energy of 600 eV and a Monkhorst-Pack k-mesh³¹ with 1 x 6 x 2 k-points for the **lp** phase and 1 x 6 x 6 k-points for the **np** phase. For COMOC-2(V), spin polarized calculations were performed in which all spins pointed in the same direction. Equilibrium configurations of the **np** and **lp** phases of DUT-5(Al)

and COMOC-2(V) were obtained by constructing a volume-energy equation of state. This required geometrical optimizations of the 4 structures at different unit cell volumes in which the cell volume was kept fixed, but the atom positions and cell shape were allowed to vary. The optimal volume was derived from a Rose-Vinet fit and a final geometry optimization at this volume was performed. The geometry optimizations were considered to be converged when the energy difference between subsequent steps was less than 10^{-7} eV. The vibrational modes and frequencies of the resulting equilibrium configurations were obtained from a normal mode analysis of the Hessian. The latter was calculated via a finite difference approach with 2 displacements of 0.015 Å for every atom in each Cartesian direction. The IR intensities of the different vibrational modes were obtained via density functional perturbation theory (DFPT)^{32, 33}.

3. Results

3.1 EPR components: spin-Hamiltonian parameters

3.1.1 lp component. As reported in Maes et al.², measuring EPR spectra of DUT-5(Al) samples doped with low V-concentration (CS-08 and CS-07) reveals two spectral components. There is one component that becomes clearly visible at lower pressures. Subtracting the EPR spectrum measured in air from that measured in vacuum yields a well-isolated EPR spectrum that we were able to simulate using a single set of spin-Hamiltonian parameters. Table 2 presents the spin-Hamiltonian parameters used for this simulation, compared to those of the different vanadyl centers in MIL-53(Al):V^{1, 19, 20}. Figure 1A contains the simulation of this component on this difference EPR spectrum for X-, Q- and W-band. Initially spin-Hamiltonian parameters were determined using X- and Q-band measurements. W-band measurements confirmed the previously determined spin-Hamiltonian parameters. The g- and A-tensors are both typical for vanadyl centers and are almost axial. There is a small tilting between the principal axes of both tensors. We labeled this component the **lp** component. More information on this assignment is presented in Section 4.1.

3.1.2 BL component. A second spectral component is visible in the EPR spectrum for the samples with low V-concentration and appears to be independent of pressure. Although it proved impossible to completely isolate this component, when the spectra are recorded on low V-concentrated samples exposed to air, the lp component is significantly broadened², making it possible to extract fairly good spin-Hamiltonian parameters for this second spectral component (see Table 2). The g- and A-tensors both are typical for vanadyl centers. However, they are now clearly rhombic, and within the experimental error there is no tilting between the principal axes of g and A. Its linewidth parameters are, as already mentioned, much larger than for lp at low oxygen partial pressure. Because of its considerably broader linewidth compared to lp at low pressure, we earlier labeled this component the broad line (**BL**) component.

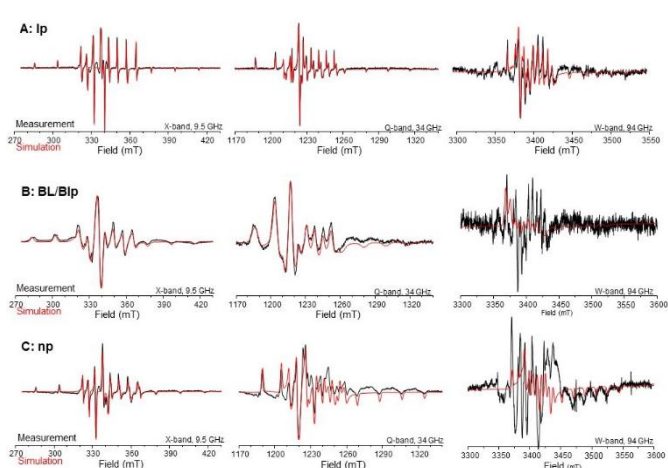


Figure 1: X-band (left, 9.5 GHz), Q-band (middle, 34 GHz) and W-band (right, 94 GHz) RT powder EPR spectra of: **A:** The **lp** component of DUT-5(Al):V: black - experiment, red - simulation. The experimental spectrum was constructed by subtracting the CS-07 EPR spectrum measured in air from the CS-07 EPR spectrum measured at 30 Pa. An anisotropic Gaussian linewidth was used for the simulations (X-band: HStrain = [13, 16, 15] MHz; Q-band: HStrain = [16, 24, 28] MHz, W-band: HStrain = [42, 48, 45] MHz). **B:** The **BL/Blp** component of DUT-5(Al):V: black - experiment, red - simulation. The experimental spectrum is the EPR spectrum of CS-07 measured in air. In W-band a Lorentzian line was subtracted. An anisotropic Gaussian linewidth was used for the simulations (X-band: HStrain = [56, 69, 57] MHz; Q-band: HStrain = [88, 130, 169] MHz, W-band: HStrain = [110, 227, 206] MHz). **C:** The **np** component of DUT-5(Al):V: black - experiment, red - simulation. The experimental spectrum was obtained by elimination of the **lp**, **BL/Blp** and Lorentz component from the CS-04 spectra measured at ambient air pressure. An anisotropic Gaussian linewidth was used for the simulations (X-band: HStrain = [21, 31, 46] MHz; Q-band: HStrain = [52, 54, 54] MHz, W-band: HStrain = [72, 83, 79] MHz).

However, as mentioned above and further explained in section 3.2, the EPR spectrum in Figure 1B contains not only the **BL** component, but also a broadened **lp** (**Blp**) one. Therefore we label this combination of two components as **BL/Blp**.

3.1.3 np component. At higher V-concentrations (from CS-05), two additional components become clearly visible: a narrow-line component with resolved HF structure labelled np (see Section 4.1 for the motivation of this labeling) and a broad Lorentzian line appearing as a background in the spectra. In order to isolate the narrow-line component we started from the EPR spectrum of the CS-04 sample measured in vacuum, where it is best visible. The EPR spectrum of the CS-07 sample measured in air (the BL/Blp component), the isolated lp component spectrum and a broad Lorentzian line were then subtracted from that CS-04 spectrum measured in vacuum. The resulting EPR spectrum was then fitted in order to extract the spin-Hamiltonian parameters. Figure 1C presents the EPR spectral component isolated in this way and its simulation in X-, Q- and W-band. The spin-Hamiltonian parameters are presented in Table 2. This isolation procedure works very well for X-band, where we were able to simulate the resulting EPR spectrum very convincingly. For Q- and W-band however, this procedure was less successful in isolating this component completely. Moreover, in W-band a lot of the spectral features of the **lp** component overlap with this component.

ARTICLE

Table 2: Spin-Hamiltonian parameter set extracted from X-, Q- and W-band EPR spectra at RT of the spectral components of DUT-5(Al):V and of the states of MIL-53(Al):V. Principal values of the g-tensor and the ^{51}V HF- (A-) tensor are shown, together with the relative Euler angles describing the tilting between the principal axes of both tensors (for their definition, see ref. ²⁵). The parameters for the **lp** component are reproduced from Maes et al. ² and the parameters for the MIL-53(Al):V states are reproduced from Nevjstić et al. ²⁰. Errors on the principal values are indicated in subscript.

Vanadyl center	g_x	g_y	g_z	A_x (MHz)	A_y (MHz)	A_z (MHz)	α (°)	β (°)	γ (°)
MIL-53(Al):V np-h 1	1.9722 ₁₀	1.9623 ₁₀	1.9316 ₁₀	164.9 _{1.0}	174.2 _{1.0}	506.4 _{1.0}	-8 ₂	-14 ₂	0 ₂
MIL-53(Al):V np-h 2	1.9713 ₁₀	1.9594 ₁₀	1.9324 ₁₀	162.5 _{1.0}	170.9 _{1.0}	504.1 _{1.0}	-8 ₂	-14 ₂	0 ₂
MIL-53(Al):V np-d	1.9719 ₁	1.9634 ₁	1.9292 ₁	165.9 _{1.0}	173.0 _{1.0}	505.7 _{1.0}	-8 ₂	-14 ₂	0 ₂
MIL-53(Al):V as	1.9725 ₁₀	1.9669 ₁₀	1.9391 ₁₀	163.0 _{2.0}	165.0 _{2.0}	492.0 _{2.0}	-8 ₂	-12 ₂	0 ₂
MIL-53(Al):V lp	1.9724 ₁	1.9675 ₁	1.9387 ₁	165.6 _{1.0}	164.3 _{1.0}	495.5 _{1.0}	0 ₂	-11 ₂	0 ₂
DUT-5(Al):V lp	1.9729 ₅	1.9685 ₅	1.9391 ₅	167.3 _{3.0}	165.7 _{3.0}	495.5 _{3.0}	0 ₂	-10 ₂	0 ₂
DUT-5(Al):V np	1.9717 ₁₀	1.9637 ₁₀	1.9278 ₁₀	165.0 _{5.0}	174.9 _{5.0}	510.1 _{5.0}	-12 ₂	-13 ₂	0 ₂
DUT-5(Al):V BL	1.9765 ₁₀	1.9742 ₂₀	1.9399 ₁₀	190.5 _{5.0}	165.6 _{5.0}	517.7 _{5.0}	0 ₂	0 ₂	0 ₂
DUT-5(Al):V BL/Blp	1.9770 ₁₀	1.9722 ₂₀	1.9401 ₁₀	184.5 _{5.0}	165.6 _{5.0}	509.7 _{5.0}	0 ₂	0 ₂	0 ₂

3.1.4 Lorentz component. The very broad Lorentzian line visible in the spectra increases in amplitude and intensity and gets narrower as the V-concentration increases. No HF structure is resolved in this spectral component. It also has a more prominent contribution to the spectrum as the microwave frequency increases. In W-band this component dominates the spectra even at low V-concentration. Table 3 contains the g-value and linewidth parameter of the fit of this Lorentzian component for the samples measured in X-, Q- and W-band at 30 Pa. The parameters for the spectra measured in air are very similar. The average g-value of this line is slightly different in X-band compared to Q- and W-band, with average g-values of 1.9712, 1.9638 and 1.9659 respectively. The large negative g-shift suggests that this spectrum is also vanadyl-related. These g-values are very close to the isotropic g-value of 1.964 reported for COMOC-2(V) in Q-band [22]. A more detailed discussion on the origin of this Lorentz component is given in Section 4.2.

Interestingly, the linewidth of this component decreases with increasing V-concentration. At low V-concentration and low frequency the linewidth is very large, making it almost impossible to detect. Therefore no values for the CS-07 sample are presented in Table 3. For samples CS-06 and CS-05 the linewidth is very similar, probably equal within experimental error. This would a priori be expected in view of the very similar global V-concentrations of the two samples. The CS-04 and CS-

03 samples have a much smaller linewidth parameter. Moreover the component is now dominant in the spectrum. Therefore CS-03 has not been measured in W-band. In samples CS-01 and CS-02 the spectrum is dominated by the EPR component of COMOC-2(V), which also lacks resolved HF structure, but has a narrower linewidth and significant g-anisotropy ². The signals from the other components are hardly discernable in the spectra of these samples. Therefore, we focused on the DUT-5(Al) samples with lower V-concentration. For sample CS-03 at the higher microwave frequencies a single Lorentzian line shape becomes less accurate in reproducing this component, see Figure S2, supporting information. Very probably g-anisotropy starts to play a significant role, like it does for the samples with even higher V-concentration. This in part also explains our difficulties of isolating the **np** component at the higher frequency bands.

Table 3: Full Width at Half Maximum (FWHM) and g-value of a Lorentzian line shape fitted to the EPR spectrum of CS samples measured at 30 Pa and RT. Left: X-band (9.5 GHz), middle: Q-band (34 GHz), right: W-band (94 GHz).

Sample	X-band		Q-band		W-band	
	g	FWHM (mT)	g	FWHM (mT)	g	FWHM (mT)
CS-06	1.9720	70	1.9647	68	1.9680	75
CS-05	1.9774	72	1.9655	67	1.9657	70
CS-04	1.9687	40	1.9623	44	1.9640	61
CS-03	1.9668	24	1.9627	29	-	-
Average	1.9712		1.9638		1.9659	

3.2 Additional samples: EPR measurements

To further unveil the origin of the paramagnetic species in DUT-5(Al):V, four additional samples were synthesized: T-VOSO₄, T-VCl₃, S-DMF-01 and S-DMF-02. Details about these samples are described in Section 2.1.

For sample T-VOSO₄, we dispersed VOSO₄•H₂O dopant salt in DUT-5(Al) under conditions where we expected the vanadium ions to enter the framework pores, but not to substitute Al-OH units in the framework. Measuring the EPR spectrum of this sample, there was no difference observed between the spectra measured in air or in vacuum. Its spectrum, shown in Figure 2B, is very similar to the spectrum of CS-07 measured in air. Upon comparing both, we found that the T-VOSO₄ EPR spectrum (red curve) perfectly fits into the spectrum of the CS-07 sample (BL/Blp, black curve) and combined with a broadened spectrum of the lp component (blue curve), it is almost identical to the CS-07 EPR spectrum, as can be seen in Figure 2A. The EPR spectrum of T-VOSO₄ is thus the pure BL component. The spin-Hamiltonian parameters presented in Table 2 confirm that the parameters determined from the spectrum of CS-07 in air for the BL/Blp component are very close but not equal to those from T-VOSO₄ for the BL component.

Sample T-VCl₃ was made exactly like the CS-08 sample, except we used VCl₃ as a dopant molecule instead of VOSO₄•H₂O. For this sample we expect that the vanadium dopant ions substitute for framework cations. They might enter as V^{III}-OH or as V^{IV}=O, though. The resulting EPR spectrum (that shows the part of the vanadium ions that have entered in the +IV oxidation state) is shown in Figure 2C. Like for the CS-08 sample, the EPR spectrum is the superposition of the BL spectrum and a weak lp component. Interestingly, using only these two components does not completely reproduce the measured spectrum. Decomposition of this EPR spectrum (see Table S4 and Figure S11 in supporting information), as explained in the next section, revealed that the BL/Blp component is responsible for the major part of this spectrum and that the sharp features present in the EPR spectrum measured at 30 Pa are coming from the lp component as expected. However, the sharp features visible in the spectrum measured in ambient air are originating from a np component, with about half of the intensity of the lp component. So both open and closed pore structures are present at very low V-concentrations with the VCl₃ dopant salt precursor, while the open pore structure is almost exclusively

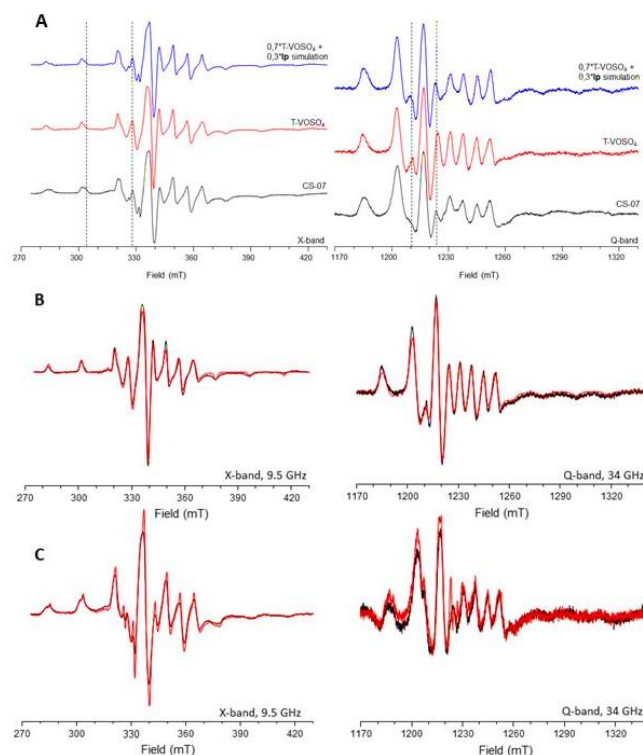


Figure 2: X-band (left, 9.5 GHz) and Q-band (right, 34 GHz) RT powder EPR spectra of: A: CS-07 measured in air (black), T-VOSO₄ measured in air (red) and a linear combination of 70% T-VOSO₄ and 30% simulated lp component (blue). The simulated lp component spectrum has a 4.5 times increase in linewidth to account for the broadening of this spectral component by O₂ in air, based on predictions from the oxygen dependency studies². B: T-VOSO₄, measured under ambient air pressure: black – experiment; red – simulation. An anisotropic Gaussian linewidth was used for the simulations (X-band: HStrain = [63, 74, 59] MHz; Q-band: HStrain = [89, 113, 149] MHz). C: T-VCl₃: black – ambient air pressure, red – vacuum (30 Pa).

present at very low (<7%) V-concentrations with the VOSO₄•H₂O dopant salt as precursor.

The last two samples were frozen solutions of VOSO₄•H₂O salt in DMF. S-DMF-02 also contained the H₂BPDC linker while S-DMF-01 did not. The EPR spectrum for both S-DMF samples was the same. In Figure S1 in supporting information the Q-band EPR spectrum measured at 90 K (black) for S-DMF-02 and the simulation (red) are presented, revealing a typical vanadyl spectrum with resolved HF interactions. Almost axial g- and A-tensors were found for the S-DMF samples, without tilting between their principal axes. Although the S-DMF EPR spectrum is similar to the T-VOSO₄ spectrum, when comparing the spin-Hamiltonian parameters of both, S-DMF has a larger isotropic part of the A-tensor, g_y is also larger, but g_z is significantly smaller.

3.3 Decomposition of the CS EPR spectra

With the knowledge of the different EPR spectral components mentioned above, we can reproduce all but one component in the experimental EPR spectra. The only exception is the broadened lp, since its linewidth depends on the (oxygen) pressure. It is to some extent always present in all spectra, both at lower and ambient air pressures. Therefore reproduction of the measured EPR spectra of all DUT-5(Al):V samples using a

linear combination of the **lp**, **BL**, **np** and Lorentz components alone proved less convincing than when using the **BL/Blp** component instead of the **BL** component. We were able to simulate the spectra with this composite component, as presented in Figure S2 in supporting information. Still the best results were obtained for the spectra measured at 30 Pa, where the broadened **lp** component interferes the least.

An example of a decomposition of an X- and Q-band EPR spectrum recorded under vacuum conditions (sample CS-05) is shown in Figure 3A, comparing the experimental with the best-fit linear combination spectrum, along with the simulated single components. For the linear combination of the simulated EPR component spectra, 6 parameters are fit to the measured spectrum. These are the multiplication factors for the simulated spectra of these four components (**lp**, **BL/Blp**, **np** and Lorentz) and two extra parameters for a straight line background correction. The simulated spectra of the **lp**, **BL/Blp** and **np** components stayed the same for all samples. The simulated Lorentz component changes for each sample, however. To properly take this into account, we divided the components simulated spectra by their calculated double integral. We use the EPR spectra as measured, so the intensity of the signal is related to the concentration of paramagnetic species, in this case vanadyl ions. These multiplication factors can thus be used to estimate the contribution of each vanadyl ion type to the total sample spectrum. Since mass and position of the sample in the spectrometer are crucial for comparison and this is most easily controlled in X-band, we will focus on this frequency band. The multiplication factors as a function of the vanadium concentration of each component for samples CS-07 to CS-03 as measured in X-band are shown in Figure 3B. The trends observed in Q-band are presented in Figure S3 and Table S1 in the supporting information. The differences with X-band can be explained by the increased difficulties in Q-band to control the mass of the samples, making the absolute factors less meaningful for comparison between samples than in X-band.

The first thing to notice is that the contribution of the Lorentzian line to the spectrum increases with V-concentration, as is directly visible in the measured spectra. The Lorentzian line rises very rapidly, dominating all other components starting from CS-04. As a result of this, adding all four components together for each concentration gives a curve with exactly the same shape as the curve for the Lorentz component. As will be explained in section 4.2, we link this Lorentz component to interacting vanadyl centers. For the other components, which are presumably isolated vanadyl centers, we expect a rise in intensity with increasing V-concentration, up to the point where close-by vanadyl centers become abundant and the intensity of the Lorentz component grows at the expense of the others. Indeed, for the **lp** and **np** components we observe a maximum in the contribution for sample CS-04, corresponding to 23 % V. Assuming a completely random distribution of V centers in the metal-OH chains, the concentration of V nodes with two neighboring Al nodes reaches a maximum at 33 % V. The **BL/Blp** component however appears to be present in each sample, approximately with the same multiplication factor of around 200. The only exception is the significantly lower factor for

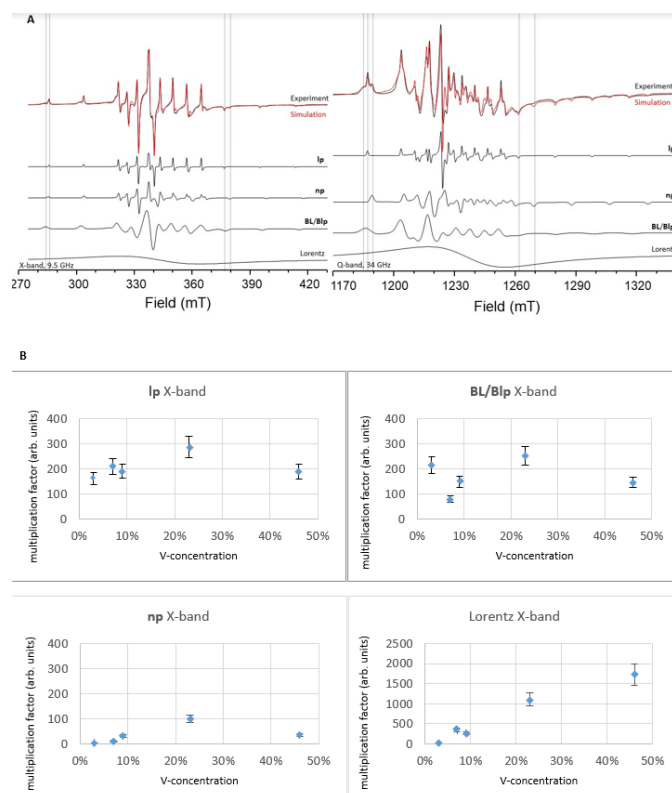


Figure 3: A: Decomposition of the CS-05 X- and Q-band (34 GHz) RT powder EPR spectrum measured in vacuum ($p \approx 30$ Pa). The linear combination of the simulated spectra of the **lp**, **BL/Blp**, **np** and Lorentz components, visible beneath the experimental spectra, convincingly reproduces the experimental spectra. An anisotropic Gaussian linewidth was used for the **lp**, **BL/Blp** and **np** simulations (see previous figures). B: Simulated contribution of each component as a function of the vanadium concentration (compared to the combined V and Al concentration, as measured by ICP-MS³) of the CS samples for the X-band 30 Pa measurements. Each simulated component was multiplied with these factors to reconstruct the total measured X-band EPR spectrum. Calculated relative error, based on repeated measurements, was 15% for all components.

BL/Blp in the CS-06 sample, accompanied by larger contributions of the **lp** and Lorentz components than expected from the general trends observed in Figure 3B. In Section 3.5 the special position of sample CS-06 will be further discussed. The **np** component has in general a smaller multiplication factor compared to the ones of **lp** and **BL/Blp**, and the relative changes of this factor as a function of V-concentration are larger.

3.4 ENDOR measurements

To probe the direct surroundings of the vanadyl centers more directly, ENDOR measurements were performed on all samples. Q-band 10 K powder ENDOR spectra measured at 1218 mT around the Larmor frequency of ^1H ($I = 1/2$) are shown in Figure 4 for CS-05 and 1 % V-doped MIL-53(Al) **as** (as synthesized), as measured by Nevjestic et al.¹. Similar, albeit weaker, ENDOR spectra have been measured for the **np** state of MIL-53(Al):V²⁰. For both ENDOR spectra shown in Figure 4 similar transitions are visible, as shown by the arrows. These transitions were attributed to the nearest proton (hydroxyl) and four sets of four (approximately) equivalent protons on the BDC/BPDC linkers of the V^{IV} ion. Since the only difference between both samples is

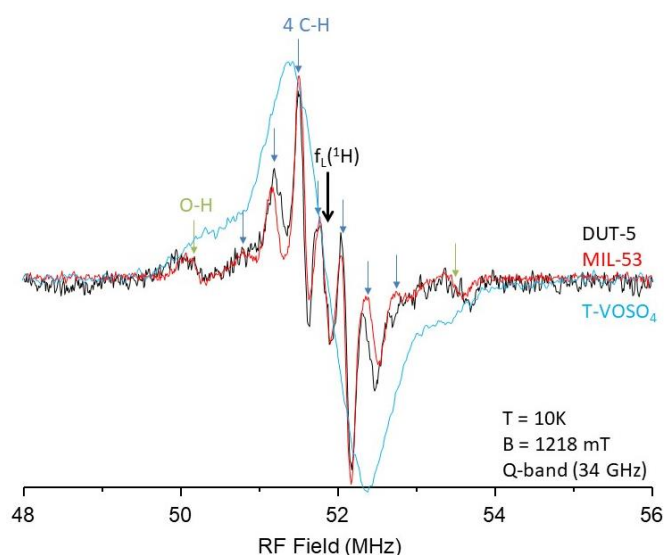


Figure 4: Q-band (34 GHz) 10K powder ^1H ENDOR spectra of CS-05 (black), 1% MIL-53(V as (red) and T- VOSO₄ (blue). Proton Larmor frequency and assignment of transitions linked to bridging OH and the BPDC linker are indicated (identifications based on Nevjestic et al.¹).

the longer linker molecule for DUT-5(Al), the nearest protons are in essence the same for both samples, explaining the similarity of the ENDOR spectra. This ^1H ENDOR signal is readily detected in all DUT-5(Al):V samples, from CS-08 with 1 % V doping until even CS-03 with 46 % V, which we did not a priori expect for the high V-concentrations.

An ^1H ENDOR measurement of T-VOSO₄ (blue) is also shown in Figure 4. Two lines are visible around the intense line at the ^1H Larmor frequency. The total ENDOR signal is simulated using only one proton interaction with a very broad linewidth, as shown in Figure S4 in supporting information. Comparing this ^1H ENDOR spectrum to the ^1H ENDOR signal of the CS samples shows that the total range is about the same for both. The BL component, which is pure in T-VOSO₄, is also present in all CS samples, so it is possible that its ^1H ENDOR signal is also present as a weak background in the ENDOR spectra for the CS samples (see Figure 4).

As for the case of MIL-53(Al):V there are also ENDOR transitions visible for the CS samples around the Larmor frequency of ^{27}Al , see Figure 5A. However the signal to noise ratio is very low. These transitions are well simulated using the same A-tensor parameters as for as MIL-53(Al):V¹, see Figure 5B. For T-VOSO₄ only a weak ^{27}Al ENDOR signal was visible exactly at the Larmor frequency, as shown in Figure 5C. Such a matrix ENDOR signal, corresponding to an interaction with distant ^{27}Al nuclei with negligible HF interaction strength ($A \approx 0$ MHz), is not observed in the spectra of lp and of vanadyl centers in MIL-53(Al):V. On the other hand, an interaction with ^{27}Al nuclei at the Al-Al framework cation distance is missing in the T-VOSO₄ ENDOR spectrum.

3.5 SEM-EDX

To further investigate the origin of the spectral components, especially BL, SEM-EDX measurements were performed. Figure S5 in supporting information shows the SEM images of the CS

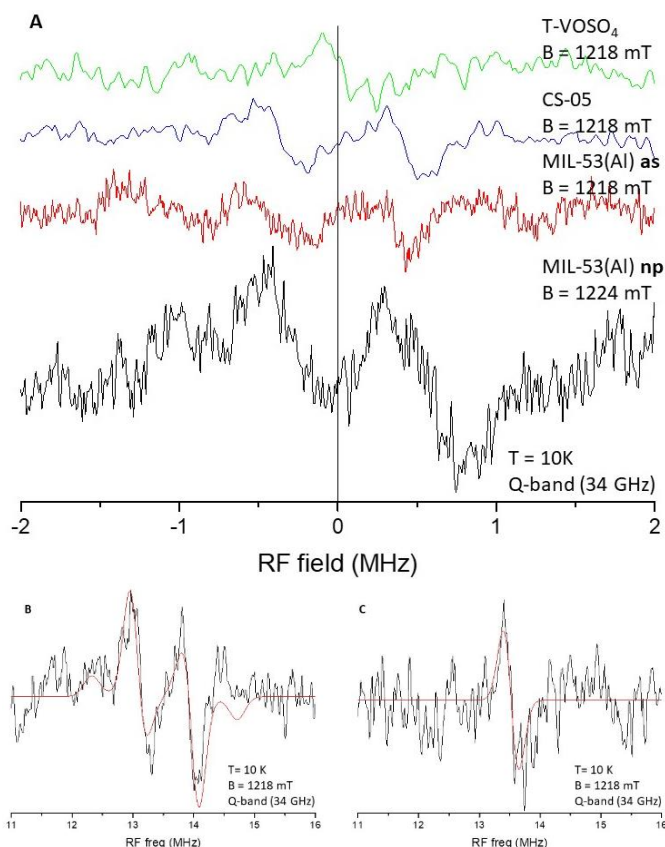


Figure 5: Q-band (34 GHz) 10K powder ^{27}Al ENDOR spectra of: A: T-VOSO₄ (green), CS-05 (blue), MIL-53(Al):V as (red) and MIL-53(Al):V np (black). The ^{27}Al Larmor frequency is indicated. MIL-53(Al) ENDOR spectra are reproduced from Nevjestic et al.¹. B: CS-05. Black - experiment, red - simulation. Simulation of the ^{27}Al ENDOR of CS-05 was performed with parameters identical to those used for MIL-53(Al):V as¹. A-tensor and linewidth parameter: $A = [-1.0, -1.0, 2.4]$ MHz, $Lw = 0.3$ MHz. C: T-VOSO₄. Black - experiment, red - simulation. A-tensor and linewidth parameter: $A = [0, 0, 0]$ MHz, $Lw = 0.3$ MHz.

samples and COMOC-2(V). A collection of sphere-like structures is visible for the samples with low V-concentration, which is in accordance with the SEM images presented in Senkovska et al.¹². Considering the evolution with increasing concentration, the SEM images show spheres that grow bigger and at the same time 'spike-like' wires start growing around them. At high vanadium concentrations the individual spheres start to clump together into larger units.

For a homogeneous dopant distribution, we expect to find Al/V ratios inside the DUT-5 crystallites with EDX that – roughly – correspond to the global Al/V ratios of the sample measured by ICP-MS³. This is the case for most of the samples, see Table S2 in supporting information. However, for the CS-06 sample we observed important deviations. The V-concentration in the spheres is lower than the global concentration. Moreover, on the SEM images bright spots are visible between the spheres, see Figure S5 in supporting information. EDX demonstrates that these have up to 75 % V-concentration (compared to the detected Al concentration), resulting in a lower V-concentration (around 4.5 %) inside the spheres than expected from ICP-MS. These clusters with high V-concentration could explain the increased presence of the Lorentz component as shown in the decomposition. However, one would then expect the other

components to be less present than expected. This is the case for the **BL/Blp** and **np** components, but not for the **lp** component, which is even more present than expected. Looking at the EDX mapping of the CS-05 sample, there are no regions with high V-concentration visible. The concentration seems homogeneously distributed over the sample and is equal to the measured ICP-MS concentration. The same agreement with ICP-MS, within the experimental error, is also observed for the other CS samples. Only the higher V-concentrated samples are less homogeneous, as reflected by their higher experimental error. Excluding sample CS-06, no grains or regions are detected that contain large amounts of vanadium and they were also not revealed by the TEM experiments of Depauw et al.³ There is also no evidence of COMOC-2(V) grains growing in the samples or any sign of a concentrated vanadium phase that we could link to the Lorentz component at higher V-concentration (see section 4.2). Furthermore, no other material can be discerned between the MOF grains, except for the vanadium-rich clusters in CS-06.

3.6 FTIR

We have used FTIR spectroscopy to detect if/which guest molecules remain in the framework pores after synthesis. A full determination of the framework IR peaks for the CS samples can be found in supporting information and was made based on first principles calculations and literature data (Hoffman et al.³⁴ for the isorecticular MIL-53(Al), Senkovska et al.¹² for DUT-5(Al), Depauw et al.³ for COMOC-2(V) and Sienkiewicz-Gromiuk and Rzączyńska³⁵ for H₂BPDC). Figures S6 and S7 in supporting information show the evolution of the framework IR bands as a function of V-concentration. The IR spectra of T-VOSO₄ and T-VCl₃ are similar to CS-08. All samples show IR bands related to free or unreacted linker molecules. Apart from the characteristic band between 2400 and 3200 cm⁻¹, two bands can function as a fingerprint for this linker molecule. Around 1700 cm⁻¹ there is the CO stretch of the free COOH group and around 1300 cm⁻¹ there is a characteristic CH bend band (a* and b* in Figure S6 respectively). These bands are most pronounced in COMOC-2(V) and the samples with high V-concentration. The first principles calculations are presented in Figure S9 and assignment of IR active peaks are presented in Table S3.

Based on the differences in the simulated IR spectra of the **np** and **lp** phases, it is possible to estimate the contribution of each phase to the total experimental IR spectrum. These differences are best visible in the antisymmetric stretching vibration of the CO₂ unit around 1600 cm⁻¹, which is red-shifted for the **np** phase compared to the **lp** phase (see Table S3). Figure S8 in supporting information shows the evolution of this CO₂ antisymmetric stretching IR band with increasing V-concentration. For the lowest V-doped sample CS-08 the largest part consists out of the **lp** phase, but the shoulder suggests that also some **np** phase is present. With increasing V-concentration the IR band of the **np** phase increases in intensity, while the opposite is true for the **lp** phase band. For the CS-04 sample the **np** phase IR band is dominant, suggesting that the majority of the MOF is in the **np** phase. For sample CS-03 an abrupt change in the IR spectra

is observed. The antisymmetric stretch vibration of the CO₂ unit now shows a blue-shift, which indicates that the structure is mainly in the **lp** phase. The abrupt change from **np** to **lp** might be caused by the increased amount of residual linker in the pores of the CS-03 sample, as visible by the more intense IR band around 1680 cm⁻¹. This may hinder the contraction of the pores and, consequently, the sample stays in the **lp** phase. These estimations are in agreement with the XRD data presented in Figure S12 in supporting information and the XRD data presented in Depauw et al.³⁶ This analysis is also consistent with observations in EPR where the relative contribution of **np** to **lp** rises for concentrations up to 23 % V.

3.7 Annealing experiment

Earlier thermogravimetric analysis (TGA) measurements on the CS samples³ had revealed a mass loss step around 600 K well below the final step corresponding to the disintegration of the framework. Therefore, we annealed the samples T-VCl₃, CS-08, CS-07 and CS-05 to try and empty the pores. The CS samples were kept at an elevated temperature of 525 K for 14 hours, T-VCl₃ at 425 K for 16 hours. A weight loss around 30% was found for all calcined samples, yet we do not expect vanadium ions being lost during the calcination. Figure 6 shows the FTIR and X-band EPR measurements on samples CS-08-H and CS-05-H (suffix H: after annealing). The measurements on the other two samples are presented in Figures S8 and S9 in supporting information. The FTIR measurements confirm that free linker molecules are removed from the pores by heating of the sample. The peak at 1700 cm⁻¹ has decreased in intensity, as indicated by the arrow. Similar loss of linker molecules were measured in FTIR after activation of MIL-53(Al):V³⁷.

The intensity of the EPR spectra increases for all samples after the calcination process. This can be explained by an increase of vanadium in the +IV state through oxidation of the EPR silent V^{III} present in the sample. Furthermore, interesting changes in the EPR spectra occur. First of all, a new intense isotropic peak appears in all spectra at $g \approx 2.004$, possibly originating from a carbon-centered radical formed during the calcination. Secondly, it is still possible to perform a decomposition of the EPR spectra of samples with low V-concentration after calcination with the same spectral components and the addition of the isotropic line. An small increase in the contribution of the **np** component is observed after calcination. Emptying the pores could thus result in formation of the closed pore state of DUT-5(Al), at least for some parts of the MOF. The **lp** component increases in intensity as expected by the general increase in intensity of the EPR spectra, while its shape appears unaltered. The intensity of the **BL/Blp** component remains or even decreases slightly. For the CS-05-H sample however, the spectrum simulated with known **lp**, **BL/Blp** (or **BL**), **np** and Lorentzian components does not completely fit the experimental spectrum (see Figure S11 in supporting information). The linewidth of the **BL** appears to have increased, as can be seen at the low-field side of the CS-05-H EPR spectrum in Figure 6A. Previous TGA measurements have shown that

samples with higher V-concentration decompose at lower temperatures, which could already be partially the case here.

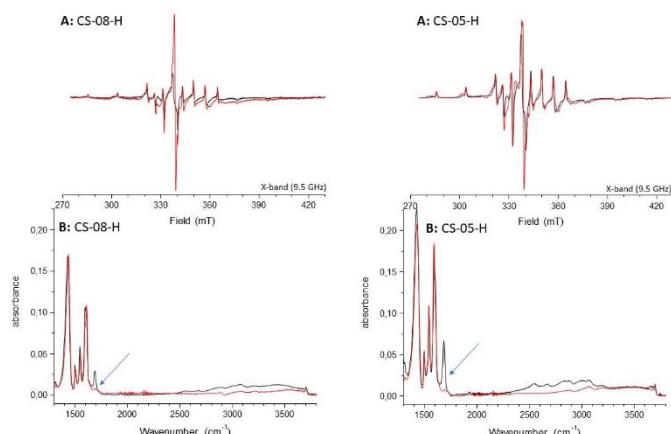


Figure 6: A: X-band (9.5 GHz) RT powder EPR spectra of CS-08 (black, left), CS-08-H (red, left), CS-05 (black, right), CS-05-H (red, right). All spectra are measured in vacuum (30 Pa). B: Attenuated total reflection FTIR spectra of CS-08 (black, left), CS-08-H (red, left), CS-05 (black, right), CS-05-H (red, right). The arrows indicate the carboxyl stretch peak around 1700 cm⁻¹ typical for the free linker molecules, which decreases in intensity after calcination.

4. Discussion

4.1 Origin of the *lp* and *np* components

The spin-Hamiltonian parameters of the *lp* component in DUT-5(Al):V and the *lp* state in MIL-53(Al):V are similar. The anisotropy of the *g*-tensor of these two centers is nearly identical, only the isotropic *g*-value in DUT-5(Al) is slightly higher than in MIL-53(Al). At the same time, the ⁵¹V A tensor in DUT-5(Al) is slightly more rhombic. The tilting between *g*- and A-tensors in the two MOFs is within experimental error identical. Furthermore, we discovered a similar broadening of the EPR spectrum of this component and the spectrum of the *lp* state of MIL-53(Al):V by the presence of (oxygen in) air ².

Additionally, as shown earlier in Section 3.4, the ¹H and ²⁷Al ENDOR interactions of the CS samples are the same as those measured for *as* MIL-53(Al):V. The ENDOR signal measured for the CS samples should be attributed to the *lp* EPR signal. In principle there might be ambiguity because these samples contain multiple vanadyl centers. However, the same ENDOR signal was observed for all CS samples, also for those with low V-concentration, that only have appreciable concentrations of *lp* and *BL*. Furthermore, for the T-VOSO₄ sample that exclusively contains *BL* centers, clearly distinct ENDOR signals were measured. For MIL-53(Al):V we related the *lp* state to a vanadyl ion at a metal node in the open pore structure. More precisely, an Al-OH framework unit is replaced by V^{IV}=O ^{1, 19, 20}. Because of the evidence provided above, the EPR signal of the *lp* component can be identified as a similar substitutional V^{IV}=O center as in large pore MIL-53(Al):V.

For the *np* component the spin-Hamiltonian parameters are almost identical to those of the *np-d* state in MIL-53(Al):V. This is remarkable, since no closed pore form of DUT-5(Al) has been

reported after synthesis in DMF ^{12, 21}. Re-examination of the XRD results on the mixed-metal MOFs, as shown in Figure S12 (supporting information), revealed low intensity diffraction peaks emerging at higher V-concentrations. To identify these features we calculated the diffraction angles for both the *lp* and *np* states using the crystallographic data of DUT-5(Al) ³⁸ and COMOC-2(V) ²², see Table S5 in supporting information. The calculated angles for a *np* state correspond to the angle at which the low intensity diffraction peak is visible. Thus these XRD data point towards a closed pore state, detectable at relative low ($\geq 7\%$) vanadium concentration ². Therefore we propose that the *np* EPR component originates from a V^{IV}=O center similar to the *np* state in MIL-53(Al):V. The fact that the spin-Hamiltonian parameters are almost equal to the *np-d* state parameters and not to those of the hydrated state, can be explained by the fact that the DUT-5(Al) framework hardly exhibits H₂O adsorption ¹².

4.2 Origin of the Lorentz component

As already mentioned in section 3.1.4, a very broad (nearly) isotropic Lorentzian line is visible in the EPR spectra, with a *g*-value comparable to the isotropic *g*-value of COMOC-2(V). Because of this similarity, one could assume this component to originate from COMOC-2(V) grains/regions in the mixed-metal MOF. However, if this would be the case, the narrower EPR spectrum of fully V-concentrated COMOC-2(V) would become visible and grow in intensity. Yet, the Lorentz component present in EPR spectra at low V-concentration has a much larger linewidth. It rapidly increases in intensity and gets narrower as the V-concentration increases, ultimately resulting in the spectrum of COMOC-2(V).

A similar Lorentzian line was observed for the MIL-53(Al):V to MIL-47(V) series by Kozachuk et al. ³⁷, but only after activation of the VCl₃ doped samples. Before activation, almost no EPR signals were visible for the high (> 5 %) V-concentrated samples, suggesting that most vanadium ions were present in the V^{III} oxidation state. Only after activation a single broad EPR signal appeared, growing in intensity with increasing V-concentration. For the MIL-53(Al):V sample with 29 % V in that study, an EPR spectrum with resolved HF structure appeared on top of the broad single line, comparable to our CS-04 and CS-03 samples. This narrowing of the linewidth at higher V-concentrations can be explained by considering exchange coupled systems ³⁹. The Lorentz component most likely appears in the EPR spectrum at low V-concentration, when two or more vanadyl centers are close enough to each other to exhibit a dipolar coupling between their magnetic moments. For simplicity only incorporated vanadium ions at a metal node will be considered. DFT calculations on MIL-47 showed that interactions within the metal-oxide chain between vanadium ions are about 100 times stronger compared to the interactions between vanadium ions on two different neighboring chains ⁴⁰. Therefore we can assume that only the intra-chain interactions affect the Lorentz component spectrum in EPR. These dipolar interactions give a broadening of the EPR lines, resulting from the sum of individual, sharper transitions around their center. When two vanadyl centers are so close to each other that they form a weak

bond, an additional interaction occurs, called the exchange interaction. At low V-concentrations, when the vanadyl centers are scattered across the MOF, the dipole interaction dominates the exchange interaction, leading to a very broad EPR line. As the V-concentration increases and more vanadyl centers are close to each other, the exchange interaction starts to dominate the dipole interaction, resulting in a regime called exchange narrowing, reducing the EPR linewidth. Thus the initial broad EPR line ultimately evolves into the COMOC-2(V) EPR signal, yet at low V-concentrations it is quite different from it. As already mentioned in Sections 3.3 and 3.5, the higher amount of the Lorentz component in sample CS-06 could be explained by the clusters with increased V-concentration observed with SEM-EDX in this sample.

4.3 Origin of the BL component

The spin-Hamiltonian parameters of the **BL** component are unlike any of the spectral components in MIL-53(Al):V, all assigned earlier to substitutional centers. The principal g-values are significantly larger compared to the other components in both MIL-53(Al):V and DUT-5(Al):V, as is the x principal value of the A-tensor. The A_z -value is close to that for the **np** state in both V-doped frameworks. The ^1H and ^{27}Al ENDOR interactions detected for substitutional $\text{V}^{\text{IV}}=\text{O}$ centers at Al-OH nodes along the chain are not seen. Furthermore, only smaller (matrix) ENDOR interactions are observed, which are absent for the $\text{V}^{\text{IV}}=\text{O}$ centers in Al-OH nodes. These results suggest that the **BL** vanadyl center is not substituting Al-OH in the framework. The appearance of **BL** as the only component in the spectra of T-VOSO₄, where we do not expect cation exchange to take place, is in line with this view.

XRD data show no evidence for other phases than the synthesized MOFs. SEM-EDX images also give no indications of other phases, except for the CS-06 sample with the highly V-concentrated particles between the MOF grains, but this sample does not exhibit an increased contribution of the **BL** EPR component. SEM-EDX does show changes in morphology of the samples with increasing V-concentration, but this is not reflected in the **BL/Blp** contribution derived from the EPR spectrum decomposition as a function of V-concentration. These data thus indicate that the vanadyl center responsible for the **BL** EPR component is present inside the MOF, but the EPR and ENDOR analysis above does not point at substitutional positions. This leaves the framework pores as most plausible location for the **BL** centers.

The next question concerns the identity of the (vanadyl) molecule inside the framework pores. A tempting hypothesis is that of a molecule containing $(\text{V}^{\text{IV}}=\text{O})^{2+}$ participating in the synthesis and left behind in the pores, with unreacted VOSO₄ as an obvious candidate. However, no VOSO₄ is involved in the synthesis of the T-VCl₃ sample, which still exhibits a prominent **BL** signal in its EPR spectra. Thus, the molecule producing the **BL** EPR spectrum cannot be VOSO₄.

A next candidate is vanadyl ions bound to free linker molecules residing in the pores. However this hypothesis was contradicted by our FTIR measurements, where an increase of free linker

molecules in the pores of the MOFs with increasing V-concentration was not accompanied with an increase of the **BL** component. Moreover, heating of the sample removes the unreacted linker molecules inside the pores, but does not decrease the **BL** EPR component in a similar way. The molecule responsible for the **BL** component is thus too strongly bound to the framework (pores) to be removed by heating of the sample. Using even higher temperatures is not possible, since disintegration of the MOF then sets in.

Because we do not observe a **BL**-like component in the EPR spectrum of MIL-53(Al):V, we looked into the differences between both MOFs, the most obvious being the larger linker molecule in DUT-5(Al). A larger linker molecule leads to somewhat larger pores and a wider variety of possible defects and defect sites. From the synthesis perspective, a second important difference between the MOFs is the solvents from which they are grown, i.e. deionized water for MIL-53(Al) and DMF for all DUT-5(Al) samples. Therefore, the **BL** component could originate from a $(\text{V}^{\text{IV}}=\text{O})^{2+}$ center coordinated with DMF molecules. Coordination of metal centers with DMF has been reported for MOFs⁴¹. As mentioned in Section 3.2, the DMF frozen solution EPR spectrum originates from a typical vanadyl, very similar to the **BL** EPR spectrum, only the total width is slightly larger. This could be explained by the difference in the environment. Alternatively it is important to note that there are two decomposition reactions possible during the synthesis of the MOF and also during calcination. DMF is known to decompose into CO and dimethylamine around 350 °C, but it has been reported that in the presence of metals (e.g. during MOF synthesis) the decomposition temperature is reduced significantly⁴²⁻⁴⁴. DMF also hydrolyses with water to form dimethylamine and formate⁴⁵. So interaction of $(\text{V}^{\text{IV}}=\text{O})^{2+}$ with dimethylamine is also possible. Therefore we tentatively propose $(\text{V}^{\text{IV}}=\text{O})^{2+}$ linked with DMF or dimethylamine in the pores of the MOF as the most likely candidate for the origin of the **BL** component.

Conclusions

EPR measurements of V-doped DUT-5(Al) reveal four different spectral components. At low V-concentrations the spectra are dominated by the **lp** and **BL** components. The **lp** component is clearly visible in the EPR spectrum when measured at low pressures, typically 30 Pa or lower. Comparison with V-doped MIL-53(Al) EPR and ENDOR spectra show that the EPR signal of the **lp** component can be identified as a similar substitutional $\text{V}^{\text{IV}}=\text{O}$ center as in large pore MIL-53(Al):V.

The **BL** component is always visible in the EPR spectra and appears as a pure component in the spectra of sample T-VOSO₄, yet its origin is very hard to determine. Our spectroscopic analysis points towards the framework pores for the location of the **BL** vanadyl center. We tentatively propose $(\text{V}^{\text{IV}}=\text{O})^{2+}$ linked with DMF or dimethylamine as the most likely molecular structure responsible for the **BL** spectral component.

From 7 % V, the **np** component becomes resolved in the EPR spectra. Examination of the XRD data and EPR spectra show that

the EPR signal of the **np** component can be assigned to a similar substitutional $V^{IV}=O$ center as in narrow pore MIL-53(Al):V. With increasing V-concentration a broad structureless Lorentzian line grows into the spectra, becoming dominant above 9 % V in X-band and even sooner in higher frequency bands. We link this component to interacting vanadyl centers inside the MOFs experiencing a combination of dipolar and exchange interactions leading to exchange narrowing at higher V-concentration and ultimately (> 66 % V) evolving into the COMOC-2(V) spectrum.

Upon calcination, a general increase in EPR intensity is observed related to the oxidation of EPR silent V^{III} ions and an additional isotropic line appears with $g \approx 2.004$, possibly originating from a newly formed carbon-centered radical. A small increase in the contribution of the **np** component compared to the other components is observed. This suggests that emptying of the pores results in formation of the closed pore state of DUT-5(Al), at least for some parts of the MOF.

Simulations using the determined spin-Hamiltonian parameters are in good agreement with the measured spectra for X-, Q- and W-band. Decomposition of the spectra using the simulations of all four components gives an indication of the relative contributions of these components to the EPR spectrum. As a priori expected, the **np** and **lp** components increase in abundance with increasing V-concentration, with a maximum around 23 % V, then decrease again. The **BL/Blp** component however is almost equally present in all CS samples up to 46 % V-concentration. The concentration of the Lorentzian line increases rapidly with increasing V-concentration, dominating all other components at high V-concentrations.

Conflicts of interest

There are no conflicts to declare.

Acknowledgements

The authors acknowledge Irena Nevjstić and Hannes Depauw for their pioneer work on the samples. The authors thank Olivier Janssens and Robin Petit for their help with the SEM-EDX measurements. The Research Foundation Flanders (FWO-Vlaanderen) is gratefully acknowledged for financially supporting this work (Grant No. G0048.13N and Hercules-1 project AUGÉ/13/16).

References

1. I. Nevjestic, H. Depauw, K. Leus, V. Kalendra, I. Caretti, G. Jeschke, S. Van Doorslaer, F. Callens, P. Van Der Voort and H. Vrielinck, *ChemPhysChem*, 2015, **16**, 2968-2973.
2. K. Maes, I. Nevjstić, H. Depauw, K. Leus, P. Van Der Voort, H. Vrielinck and F. Callens, *Optical Materials*, 2019, **94**, 217-223.
3. H. Depauw, I. Nevjstić, G. Wang, K. Leus, F. Callens, E. De Canck, K. De Buysser, H. Vrielinck and P. Van Der Voort, *Journal of Materials Chemistry A*, 2017, **5**, 24580-24584.
4. Z. Hu, B. J. Deibert and J. Li, *Chem. Soc. Rev.*, 2014, **43**, 5815-5840.
5. K. Leus, I. Muylaert, M. Vandichel, G. B. Marin, M. Waroquier, V. Van Speybroeck and P. Van Der Voort, *Chem. Commun.*, 2010, **46**, 5085-5087.
6. J.-R. Li, R. J. Kuppler and H.-C. Zhou, *Chem. Soc. Rev.*, 2009, **38**, 1477-1504.
7. L. E. Kreno, K. Leong, O. K. Farha, M. Allendorf, R. P. Van Duyne and J. T. Hupp, *Chem. Rev.*, 2012, **112**, 1105-1125.
8. H.-S. Wang, Y.-H. Wang and Y. Ding, *Nanoscale Advances*, 2020, **2**, 3788-3797.
9. M. Rivera-Torrente, L. D. B. Mandemaker, M. Filez, G. Delen, B. Seoane, F. Meirer and B. M. Weckhuysen, *Chem. Soc. Rev.*, 2020, **49**, 6694-6732.
10. K. Barthelet, J. Marrot, D. Riou and G. Férey, *Angew. Chem.-Int. Edit.*, 2002, **41**, 281.
11. T. Loiseau, C. Serre, C. Huguenard, G. Fink, F. Taulelle, M. Henry, T. Bataille and G. Férey, *Chem.-Eur. J.*, 2004, **10**, 1373-1382.
12. I. Senkowska, F. Hoffmann, M. Fröba, J. Getzschmann, W. Böhlmann and S. Kaskel, *Microporous and Mesoporous Materials*, 2009, **122**, 93-98.
13. S. Abednatanzi, P. Gohari Derakhshandeh, H. Depauw, F. X. Coudert, H. Vrielinck, P. Van Der Voort and K. Leus, *Chem. Soc. Rev.*, 2019, **48**, 2535-2565.
14. C. Volkringer, T. Loiseau, N. Guillou, G. Férey, E. Elkaim and A. Vimont, *Dalton Trans.*, 2009, DOI: 10.1039/B817563B, 2241-2249.
15. C. Serre, F. Millange, C. Thouvenot, M. Noguès, G. Marsolier, D. Louër and G. Férey, *J. Am. Chem. Soc.*, 2002, **124**, 13519-13526.
16. F. Millange, N. Guillou, R. I. Walton, J.-M. Greneche, I. Margiolaki and G. Férey, *Chem. Commun.*, 2008, DOI: 10.1039/B809419E, 4732-4734.
17. P. L. Llewellyn, P. Horcajada, G. Maurin, T. Devic, N. Rosenbach, S. Bourrelly, C. Serre, D. Vincent, S. Loera-Serna, Y. Filinchuk and G. Férey, *J. Am. Chem. Soc.*, 2009, **131**, 13002-13008.
18. J. P. S. Mowat, V. R. Seymour, J. M. Griffin, S. P. Thompson, A. M. Z. Slawin, D. Fairen-Jimenez, T. Duren, S. E. Ashbrook and P. A. Wright, *Dalton Trans.*, 2012, **41**, 3937-3941.
19. I. Nevjstić, H. Depauw, K. Leus, G. Rampelberg, C. A. Murray, C. Detavernier, P. Van Der Voort, F. Callens and H. Vrielinck, *The Journal of Physical Chemistry C*, 2016, **120**, 17400-17407.
20. I. Nevjestic, H. Depauw, P. Gast, P. Tack, D. Deduytsche, K. Leus, M. Van Landeghem, E. Goovaerts, L. Vincze, C. Detavernier, P. Van Der Voort, F. Callens and H. Vrielinck, *Phys. Chem. Chem. Phys.*, 2017, **19**, 24545-24554.
21. J. Wieme, K. Lejaeghere, G. Kresse and V. Van Speybroeck, *Nat Commun*, 2018, **9**, 4899.
22. Y. Y. Liu, S. Couck, M. Vandichel, M. Grzywa, K. Leus, S. Biswas, D. Volkmer, J. Gascon, F. Kapteijn, J. F. Denayer, M. Waroquier, V. Van Speybroeck and P. Van Der Voort, *Inorg. Chem.*, 2013, **52**, 113-120.
23. T. Loiseau, C. Mellot-Draznieks, H. Muguerra, G. Férey, M. Haouas and F. Taulelle, *Comptes Rendus Chimie*, 2005, **8**, 765-772.
24. R. A. Serway and S. A. Marshall, *The Journal of Chemical Physics*, 1967, **46**, 1949-1952.
25. S. Stoll and A. Schweiger, *Journal of Magnetic Resonance*, 2006, **178**, 42-55.

26. G. F. I. Kresse, J. , *Phys. Rev. B: Condens. Matter Mater. Phys*, 1996, **54**, 11169.
27. K. B. John P. Perdew, and Matthias Ernzerhof, *Phys. Rev. Lett.*, 1997, **77**, 3865.
28. S. Grimme, *J. Comput. Chem.*, 2006, **27**, 1787–1799.
29. S. E. Grimme, S.; Goerigk, L., *J. Comput. Chem.*, 2011, **32**, 1456–1465.
30. P. E. Blöchl, *Phys. Rev. B: Condens. Matter Mater. Phys.*, 1994, **50**, 17953.
31. H. J. P. Monkhorst, J. D., *Phys. Rev. B: Condens. Matter Mater. Phys.*, 1976, **13**, 5188.
32. P. B. Giannozzi, S., *J. Chem. Phys.*, 1994, **100**, 8537–8539.
33. S. D. G. Baroni, S.; Dal Corso, A.; Giannozzi, P., *Rev. Mod. Phys.*, 2001, **73**, 515.
34. A. E. J. Hoffman, L. Vanduyfhuys, I. Nevjestic, J. Wieme, S. M. J. Rogge, H. Depauw, P. Van Der Voort, H. Vrielinck and V. Van Speybroeck, *J. Phys. Chem. C*, 2018, **122**, 2734-2746.
35. J. Sienkiewicz-Gromiuk and Z. Rzączyńska, *Journal of Thermal Analysis and Calorimetry*, 2012, **112**, 877-884.
36. H. Depauw, Ghent University, 2018.
37. O. Kozachuk, M. Meilikhov, K. Yusenko, A. Schneemann, B. Jee, A. V. Kuttatheyil, M. Bertmer, C. Sternemann, A. Pöppel and R. A. Fischer, *Eur. J. Inorg. Chem.*, 2013, **2013**, 4546-4557.
38. J. Wieme, Doctor PHD Thesis, Ghent University, 2020.
39. G. D. Bencini A., *EPR of Exchange Coupled Systems*, Springer-Verlag, Berlin, 1989.
40. D. E. Vanpoucke, J. W. Jaeken, S. De Baerdemacker, K. Lejaeghere and V. Van Speybroeck, *Beilstein J Nanotechnol*, 2014, **5**, 1738-1748.
41. R. Seetharaj, P. V. Vandana, P. Arya and S. Mathew, *Arabian Journal of Chemistry*, 2019, **12**, 295-315.
42. M. A. Yiqian Wan, Mats Larhed, and and A. Hallberg, *J. Org. Chem.*, 2002, **67**, 6232-6235.
43. C. K. Brozek, V. K. Michaelis, T. C. Ong, L. Bellarosa, N. Lopez, R. G. Griffin and M. Dinca, *ACS Cent Sci*, 2015, **1**, 252-260.
44. V. A. Logvinenko, S. A. Sapchenko and V. P. Fedin, *Journal of Thermal Analysis and Calorimetry*, 2015, **123**, 697-702.
45. D. L. a. J. Comins, Sajjan P., in *Encyclopedia of Reagents for Organic Synthesis*, 2001, DOI: <https://doi.org/10.1002/047084289X.rd335>.